Journal of
MATERIALS RESEARCH

Invited Feature Paper-Review
DOI:10.1557/s43578-022-00615-0

BEYOND LITHIUM-ION BATTERIES

Rapid 3D nondestructive imaging technology for batteries: Photoacoustic microscopy

Jingying Zhou[1], Yibo Zhao[1], Huihui Liu[1], Xingye Tang[1], Sung-Liang Chen[1,3,4,a)], Shou-Hang Bo[1,2,a)]

[1] *University of Michigan-Shanghai Jiao Tong University Joint Institute, Shanghai Jiao Tong University, Shanghai 200240, China*
[2] *School of Chemistry and Chemical Engineering, Shanghai Jiao Tong University, Shanghai 200240, China*
[3] *Engineering Research Center of Digital Medicine and Clinical Translation, Ministry of Education, Shanghai 200030, China*
[4] *State Key Laboratory of Advanced Optical Communication Systems and Networks, Shanghai Jiao Tong University, Shanghai 200240, China*
[a)] Address all correspondence to these authors. e-mails: sungliang.chen@sjtu.edu.cn; shouhang.bo@sjtu.edu.cn

Received: 20 January 2022; accepted: 1 June 2022

High-specific capacity electrodes can support high-energy density batteries but lead to safety issues. To monitor the safety and reveal the mechanism behind battery failure, it is important to image and sense the changes inside a battery during cycling, which requires rapid three-dimensional nondestructive imaging technology. Photoacoustic microscopy (PAM), as a burgeoning imaging method for clinical studies, can satisfy these requirements. However, PAM has not been explored in battery applications until recently. In this review, the basic principles of PAM and batteries are explained. We outline the key challenges faced by developing high-energy density batteries, and the roles that PAM can play in related studies. Furthermore, current progress in applying PAM to batteries is summarized. In the end, we discuss possible future research directions of PAM in battery studies. Through this review, we introduce a new imaging method to the battery community and an emerging application direction for PAM experts.

Introduction

Introduction of batteries

The history of lithium-ion (Li-ion) batteries dates back to the 1970s. In 1976, Stanley Whittingham demonstrated that reversible Li intercalation reactions, in particular those of metal sulfides such as TiS_2, were conducive to the construction of rechargeable batteries, laying down a theoretical foundation [1]. Subsequently, John B. Goodenough discovered that lithium cobalt oxide ($LiCoO_2$) can be used as a high-voltage cathode material, providing higher energy density than TiS_2 and other types of sulfide materials [2]. Akira Yoshino patented the first rechargeable Li-ion batteries by combining a $LiCoO_2$ cathode with a graphite anode [3]. In 1991, Sony first commercialized Li-ion batteries [4]. As of today, Li-ion batteries have been used ubiquitously in applications ranging from portable devices to electric vehicles to large-scale energy storage devices. To further mark the importance of Li-ion batteries, Stanley Whittingham, John B. Goodenough, and Akira Yoshino were awarded the Nobel Prize in Chemistry in 2019 for their development of Li-ion batteries.

The basic working principle of Li-ion batteries is illustrated in Fig. 1 [5]. The cell consists of a liquid electrolyte, a separator, a $LiCoO_2$ cathode, and a graphite anode. The copper and aluminum are current collectors connected to an external circuit. When charging, Li ions are transported in the ionic conductive electrolyte, moving from the cathode to the anode. The cathode and anode react as follows:

$$\mathrm{LiCoO_2} \underset{\text{discharge}}{\overset{\text{charge}}{\longleftrightarrow}} \mathrm{Li}_{1-x}\mathrm{CoO_2} + x\mathrm{Li}^+ + xe^- \quad \text{(cathode)}$$

$$\mathrm{C} + xe^- + x\mathrm{Li}^+ \underset{\text{discharge}}{\overset{\text{charge}}{\longleftrightarrow}} \mathrm{Li}_x\mathrm{C} \quad \text{(anode)}$$

When discharging, the reverse reactions occur with Li ions moving from the anode to the cathode. Electrons are moved in the external circuit, powering devices, such as the light bulb shown in Fig. 1. The reversibility of the electrode reactions is the basis of rechargeable batteries.

For an electrode, the theoretical specific capacity (Q_c) refers to the total coulombs that can be provided by moving all the Li

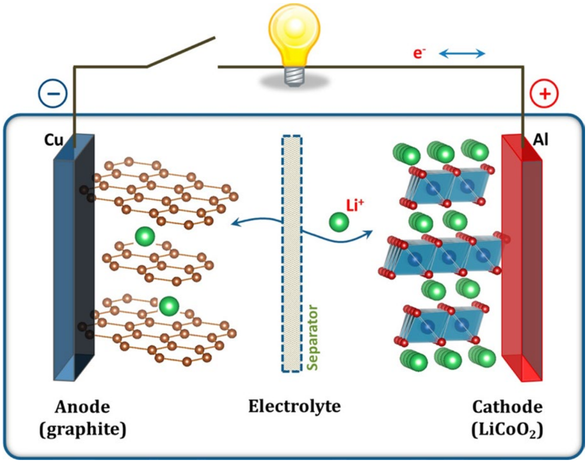

Figure 1: Schematic working principle of a $LiCoO_2$/graphite battery. Reprinted with permission from Ref. [5], Copyright 2013 American Chemical Society.

ions in and out in 1 g of the electrode material, and it can be calculated as follows:

$$Q_c = \frac{N_A \cdot q \cdot n}{M} \cdot \frac{1\,\text{mAh}}{3.6\,C} \quad (1)$$

In this equation, N_A is Avogadro's constant with a value of 6.022 × 10^{23} mol^{-1}; q is the charge of a Li-ion, which is 1.602 × 10^{-19} C; n is the maximum number of Li ions that can be used in 1 mol of the electrode material; and M is the molar mass of the electrode [6, 7]. With $n = 1$ mol and $M = 98.871$ g/mol, the theoretical specific capacity of $LiCoO_2$ is 271.039 mAh/g. Nevertheless, when charged more than 50% ($x > 0.5$), $Li_{1-x}CoO_2$ tends to decompose and generate oxygen, significantly limiting the practical specific capacity and reversibility of $LiCoO_2$ [8].

The energy density is the energy stored per unit mass of the battery, which depends on the practical capacity, the discharge voltage, and the overall mass of the battery, including that of the electrodes, separator, electrolytes, current collectors, and packaging. Based on this relationship, a cathode with a high electrochemical potential, an anode with a low electrochemical potential, and a small overall mass of the battery are important to achieve a high energy density. For instance, to achieve higher energy density, extremely thin separators were used in the Samsung Note 7. However, thin separators are more fragile and are more likely to cause safety incidents [9, 10].

Urgent problems in batteries

A graphite anode with a layered structure is widely employed in commercial Li-ion batteries but cannot sustain electrochemical abuse conditions. Li ions are topotactically intercalated into the graphite anode during charging. However, if the diffusion speed of Li ions is low in the graphite anode, a competing reaction of Li directly reducing into Li metal would occur. Such Li-metal deposition is not uniform and can form sharp dendritic structures on the graphite surface known as Li dendrites. These growing Li dendrites can penetrate the separator and cause batteries to short circuit or even explode. Especially under fast charging conditions, Li dendrites are more likely to form [9]. Mei et al. analyzed the Li deposition process on the graphite surface from the perspectives of electrochemistry and heat generation [10]. A more direct approach to monitor whether Li dendrites form and grow on the graphite surface during cycling remains needed.

In addition, the limited capacity of graphite (max. 372 mAh/g) restricts further enhancement of the battery energy density. One, of course, has the possibility to replace the graphite anode directly with a Li-metal anode, which possesses a very high specific capacity and extremely low electrochemical potential. However, similar to our earlier discussion, it remains crucial to suppress the formation of sharp Li dendrites on the Li anode during cycling. Plenty of work has been devoted to inhibiting the growth of Li dendrites. Xu et al. designed a Li/Li_3Bi anode, where the adsorption energy of the Li atoms is higher than the cohesive energy of the bulk Li, leading to homogeneous Li deposition and 250 cycles under an extremely high current density of 20 mA/cm^2 [11]. A polypropylene separator coated with ultrastrong diamond-like carbon was proposed to induce uniform Li deposition and suppress dendrite growth as well [12]. However, this problem will not be solved fundamentally until the reason for inhomogeneous nucleation and the mechanism of dendrite growth are revealed. For this, an efficient method of directly observing Li metal in batteries is significant. Optical microscopy (OM) is a convenient method with a high temporal resolution that has been used to observe Li dendrites [13, 14]; however, only two-dimensional (2D) information can be acquired. Electron microscopy can provide images with higher spatial resolution and has also been applied to observe Li dendrites [11, 15, 16]; however, it also can only offer 2D information, and the complex sample preparation makes in situ experiments very difficult. X-ray tomography has the capability of three-dimensional (3D) imaging but is time consuming, making it impractical for in situ and in operando experiments [17, 18]. In addition, Li is barely visible to X-rays due to its low electron density [19]. A more powerful imaging method for Li metal remains needed.

Besides, "dead" Li is one of the culprits of battery capacity decay and eventual failure. In batteries, the Li-metal anode contacts electronically conductive current collectors, from which Li gains or loses electrons. Ideally, Li metal deposits on one electrode when discharging, and the same amount of Li metal should be stripped when charging. In this case, the efficiency of the cell is 100%, which is practically impossible to achieve. The amount of stripped Li is almost always less than that of deposited Li. In this cycling process, Li loses through solid-electrolyte interphase (SEI) formation, galvanic corrosion, and electrically isolated Li ("dead" Li) formation. Research has shown that the "dead" Li accounts for more than 75% of the total Li loss in batteries with a liquid electrolyte [20]. Therefore, the study on "dead" Li is necessary to reveal the failure mechanism of Li-ion batteries.

On the cathode side, oxides are mainly used, including $LiFePO_4$, $LiCoO_2$, and $LiCo_xMn_yNi_{1-x-y}O_2$. At the locations where the electrochemical reactions occur, the cathode must be in contact with ion- and electron-transfer pathways. Here, electron-transfer pathways are formed by cathode particles and carbon additives, and the liquid electrolyte infiltrating into the cathode pores is responsible for ion transfer. Therefore, the porosity and tortuosity in the cathode are extremely important. To optimize the energy and power densities of batteries, one must minimize the porosity of the electrode, while, at the same time, ensuring facile ion/electron transfer on the electrode level. Porosity is also important in a graphite anode, but for a Li-metal anode, pure Li foils are used, and there is no porosity. It has been proposed that mercury intrusion can be used to measure the porosity; however, this approach is ineffective for closed pores, and mercury itself is not friendly to use at all [21]. Therefore, developing a reliable, fast, and environmentally friendly method to measure porosity is highly desired.

The degree of electrolyte wetting is also crucial for battery performance. After a cell using a liquid electrolyte is assembled, it is allowed to rest for several hours to ensure that the liquid electrolyte fully infiltrates the electrode. During the rest period, a uniform SEI should also form, as a result of the reactions between the electrodes and the liquid electrolyte. However, the optimum soaking time remains unknown; a characterization method to detect the degree of wetting is thus needed. During cycling, newly exposed electrode surfaces will be generated that consume the liquid electrolyte. As a result, the failure process of a battery is often accompanied by a decrease in the amount of liquid electrolyte [22, 23]. Weydanz et al. used neutron imaging to visualize the infiltration process of electrolytes and studied the effect of vacuum on the soaking speed and soaking time [24]; however, neutron imaging is too expensive to be applied on a large scale. Deng et al. proposed that ultrasonic imaging is capable of determining the degree of wetting in a pouch cell. However, the resolution is only on the order of millimeters [23].

Solid electrolytes can be used in next-generation batteries instead of liquid electrolytes. It can separate the two electrodes while conducting ions. In addition, the strong mechanical properties of solid electrolytes can in principle inhibit the growth of Li dendrites, enabling the application of a Li-metal anode [25]. However, solid electrolytes have been observed to crack during Li-metal battery cycling, causing battery failure. Electron microscopy and X-ray tomography have been applied to study cracks in solid electrolytes [26–28]. However, similar to the observation of Li dendrites, electron microscopy can only provide 2D information and X-ray tomography is time consuming. Therefore, alternative methods are needed to track the Li penetration, solid-electrolyte cracks, and short-circuit processes, which are fundamental to stable cycling of Li metal in solid-state systems.

To summarize, the key issues in battery research are the development of imaging methods that can observe Li dendrites, analyze "dead" Li, measure the tortuosity and porosity of the cathode, monitor the degree of liquid electrolyte wetting in the battery, and track crack propagation in solid electrolytes (Fig. 2). To this end, the imaging method should be rapid, nondestructive, and capable of 3D imaging, which remains lacking.

Introduction of PAM

Photoacoustic microscopy (PAM) is based on the photoacoustic effect. In 1880, Alexander Graham Bell first discovered that

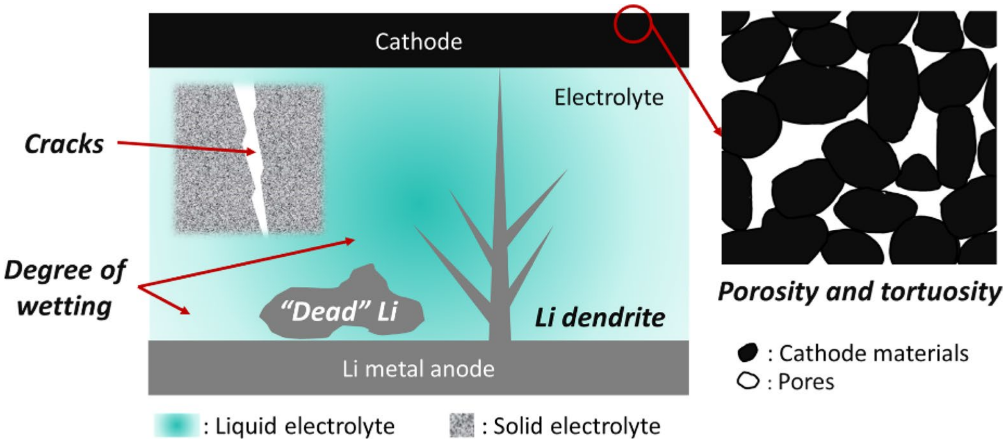

Figure 2: Urgent challenges for high-energy density and safe batteries.

sound is emitted from a solid under light illumination [29]. When a light-absorbing material is illuminated by light, the photon absorption of the material is converted into heat, causing a temperature rise and a thermoelastic volume change of the material. When a modulated or pulsed light is used, the volume change causes the initial sound pressure, which then propagates outward in the form of mechanical waves, that is, acoustic waves. Then, the acoustic waves can be detected by a hydrophone placed outside the material. In PAM, the initial acoustic pressure can be expressed by the following equation:

$$p_0 = \Gamma \cdot \zeta \cdot \mu_a \cdot F. \tag{2}$$

In Eq. (2), p_0 is the initial acoustic pressure, which is related to photoacoustic amplitude; Γ is the Gruneisen parameter; ζ denotes the heat conversion efficiency; μ_a is the optical absorption coefficient; and F is the incident light fluence. In PAM, given fixed incident light fluence (F), the initial acoustic pressure (p_0) is mainly determined by the optical absorption coefficient (μ_a), which is dependent on the materials and excitation wavelengths. Thus, the PAM image contrast is provided by different μ_a between the light-absorbing material and background material. Besides, the light-absorbing material species can be well identified by their different dependence of μ_a on excitation wavelengths (i.e., different absorption spectra) [30–32].

There are two types of PAM systems: acoustic-resolution PAM (AR-PAM) and optical-resolution PAM (OR-PAM) systems. If the sound focal spot size is smaller than the light focal spot size, the lateral resolution (defined later) of the system is determined by the former and the technique is called AR-PAM. In contrast, if the light focal spot size is smaller than the sound focal spot size, the lateral resolution is dependent on the light focal spot size and the technique is called OR-PAM [30, 31]. PAM has been extensively used in biomedical applications. In terms of deep imaging depth in light-scattering biological tissue, AR-PAM holds preponderance owing to the low scattering characteristics of ultrasound. On the other hand, OR-PAM is more advantageous in high lateral resolution. Compared with acoustic focusing, optical focusing can achieve smaller focal spot size because of relatively short wavelengths of optical waves. As a result, OR-PAM is capable of resolving detailed features. To illustrate the working principle of OR-PAM, a typical OR-PAM system is introduced. In Fig. 3(a), the configuration of a home-built OR-PAM system is shown [33]. The 532 nm laser is divided into two beams by a beam splitter (BS). One of them with lower laser energy works as a trigger signal. The other beam is focused on the sample after passing through neutral density filters (NDF1), two plano-convex lenses (L1 and L2), a reflective mirror (M), and an achromatic doublet lens (DL). A needle hydrophone is used to receive the photoacoustic signal. The receiving side of the hydrophone is submerged in deionized (DI) water rather than exposed to air because of the rapid attenuation of the typically high-frequency (tens of MHz) photoacoustic signal in gas. The DI water serves as an ultrasonic coupling medium in the PAM system. A water tank is used to hold DI water. The water tank has a thin polyethylene terephthalate (PET) membrane at its bottom, and the sample is placed below the water tank. For the same purpose, the ultrasonic coupling medium (e.g., ultrasound gel, glycerin, etc.) is added between the sample and membrane to guarantee that no air is present. A 2D motorized stage is used to move the sample for point-by-point scanning to form PAM images. It is worth mentioning that there are many different configurations to implement OR-PAM, and Fig. 3(a) is just one of them.

PAM, as a rapid 3D nondestructive imaging technology, is widely used in biomedical research and clinical diagnosis. As an example, Fig. 3(b) presents a photograph of a rat ear that was clearly imaged by OR-PAM [34]. A high-quality image of blood vessels in the ear is presented in Fig. 3(c), displayed in maximum amplitude projection (MAP) along the depth direction. The 3D

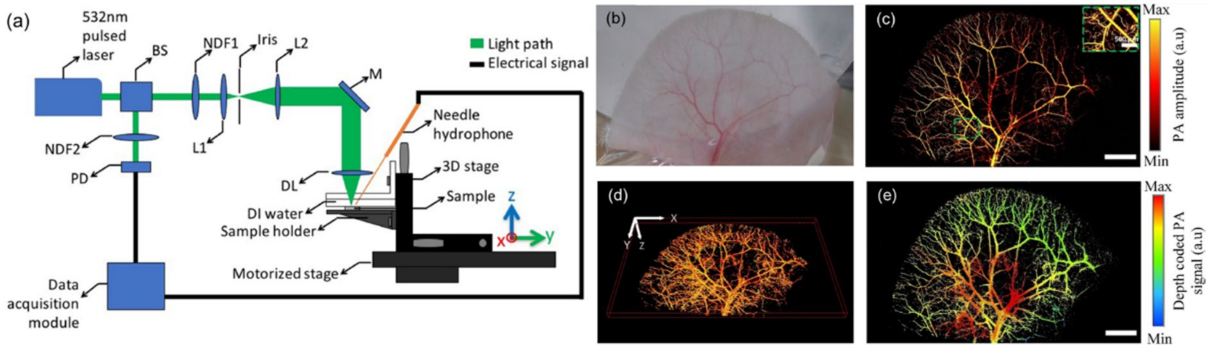

Figure 3: OR-PAM system and application in biomedical research. (a) Schematic of OR-PAM system. BS: beam splitter; NDF1 and NDF2: neutral density filters; PD: photodiode; L1 and L2: plano-convex lenses; M: reflective mirror; DL: achromatic doublet lens; DI water: deionized water. Reprinted from Ref. [33], Copyright 2020 Society of Photo-Optical Instrumentation Engineers (SPIE). (b) Photograph of a rat ear. (c) Photoacoustic MAP image of a rat ear. (d) Photoacoustic 3D image of a rat ear. (e) Photoacoustic depth-encoded image of a rat ear. PA: photoacoustic. The scale bars in the figures are 2 mm. Reprinted from Ref. [34], Copyright © 2021 The Authors.

structure and depth distribution of blood vessels are shown in Figs. 3(d) and (e), respectively. For clinical diagnosis, Jin et al. established a portable OR-PAM to visualize the vascular aberration near the tumor in oral cancer [35]. Zhang et al. demonstrated multi-wavelength AR-PAM imaging, and 3D images of the melanoma and surrounding vessels were visualized [36]. The melanin decrease in retinal pigment epithelium is a symbol of ocular function degeneration. Shu et al. employed OR-PAM with high axial resolution (defined later) and successfully realized quantitative analysis of melanin content [37]. There have been numerous articles reporting biomedical and clinical applications of PAM.

Characteristics of PAM

We first discuss the lateral and axial resolution of PAM. The spatial resolution in the x–y plane in Fig. 3(a) is called the lateral resolution. The spatial resolution along the z-axis in Fig. 3(a) is called the axial resolution. The lateral resolution depends on the size of the focal spot and is considered differently in AR-PAM and OR-PAM. In AR-PAM, the lateral resolution depends on the sound focal spot size and can be calculated using Eq. (3):

$$R_{L,AR} = \frac{0.71\lambda_a}{NA_a} = \frac{0.71v_a}{f_0 \cdot NA_a}, \tag{3}$$

where λ_a is the center wavelength of the photoacoustic signals and NA_a is the acoustic numerical aperture. λ_a is equal to the sound velocity (v_a) divided by the center frequency of the photoacoustic signals (f_0). v_a in water is approximately 1500 m/s [31, 38]. For example, the lateral resolution was estimated to be 45 μm and degraded to 120 μm when it was used practically for rat skin [39]. The lateral resolution of another fast AR-PAM was 25 and 70 μm along the two orthogonal lateral directions [40]. In OR-PAM, the lateral resolution is determined by Eq. (4):

$$R_{L,OR} = \frac{0.51\lambda_o}{NA_o}, \tag{4}$$

where λ_o is the laser wavelength and $\mathrm{NA_o}$ is the optical numerical aperture. The lateral resolution of OR-PAM can reach hundreds of nanometers to several micrometers, which is restricted by the optical diffraction limit. In 2008, OR-PAM was developed with a lateral resolution of barely 5 μm [41]. Moreover, when the wavelength of the laser was reduced to 260 nm, a lateral resolution of 700 nm could be achieved [42]. To further improve the lateral resolution, an optical objective with a large $\mathrm{NA_o}$ of 1.23 was designed and employed, and a lateral resolution as high as 220 nm at a laser wavelength of 532 nm was demonstrated [43].

The lateral resolution essentially depends on the focal spot size, whereas the axial resolution originates from the arrival-time difference of the photoacoustic signal. Along the *z*-axis in Fig. 3(a), a higher altitude indicates that the region is closer to the hydrophone and that the photoacoustic signal can be received sooner. The axial resolution depends on the bandwidth of the hydrophone (Δf) and the sound velocity (v_a) [44] and can be expressed by Eq. (5):

$$R_A = \frac{0.88v_a}{\Delta f} \tag{5}$$

The bandwidth is mainly related to the hydrophone and is determined once it is fabricated, typically ranging from 1 to 100 MHz. As an example, with a sound velocity of 1500 m/s and bandwidth of 100 MHz, the theoretical axial resolution can be calculated to be 13.2 μm. According to the calculation result, it is difficult to reach an axial resolution of less than 10 μm in practical PAM. By changing the ultrasonic coupling medium, e.g., replacing water with silicone oil, the sound velocity can be reduced to 1100 from 1500 m/s. As a result, the axial resolution can be enhanced to 5.8 μm [45]. The one-dimensional depth profile can be obtained from the time-domain photoacoustic signal acquired at one point over the lateral plane, that is, the *x*–*y* plane in Fig. 3(a). The 3D images are acquired by conducting 2D lateral scanning and reconstructing these time-domain photoacoustic signals acquired over the lateral plane. Since 3D imaging can be achieved with 2D lateral scanning, fast image acquisition for 3D imaging is feasible. Besides, the image reconstruction from raw data in PAM typically does not require complicated algorithm, allowing fast image formation. Given these advantages, PAM is ideal for in situ and in operando experiments.

Following the fast imaging discussed above, finally, we discuss the temporal resolution of PAM. The imaging speed of OR-PAM is determined by a few factors. As shown in Fig. 3(a), the imaging speed is mainly limited by the scanning speed of the motorized stage. As a result, it takes approximately 5 min to scan 256 × 256 pixels using the laser with a pulse repetition frequency of 1 kHz. To acquire a higher-quality image with high signal-to-noise ratio (SNR), multiple scans can be performed and averaged. A delicate balance between the temporal resolution, scanning area, and SNR must be made in well-planned experiments. Based on our experience, spending ~ 20 mins to repeat the scan four times can provide a high-quality image of Li metal in batteries. Note that the state-of-the-art OR-PAM systems can realize much faster imaging speed with optimized implementation of the imaging system (discussed later), and thus, the above-quoted acquisition time has much room to be shortened.

Table 1 compares PAM with other imaging methods. The comparison shows that PAM has not only a satisfactory spatial resolution but also a high temporal resolution that can support in situ and in operando experiments. In addition, PAM can achieve 3D imaging, and the imaging system is relatively easy to establish.

TABLE 1: Comparison of Different Imaging Methods.

Technology	Spatial Resolution (μm)	Temporal Resolution (s)	2D/3D	Cost ($)	Others
Optical microscopy	1	$<10^{-1}$	2D	10^{2}	Easy to access; easy sample preparation
Electron microscopy	10^{-3}	$<10^{-1}$	2D	10^{5}	High sample requirement
X-ray tomography[a]	$10^{-2}-10^{-1}$	$10^{2}-10^{4}$	3D	10^{5} – extremely high	Not sensitive to Li
Neutron imaging[b]	10	$1/10^{3}$	2D/ 3D	extremely high	Sensitive to Li
Ultrasonic imaging	10^{2}	10^{2}	3D	10^{4}	High penetration depth
PAM	1	$10^{1}-10^{2}$	3D	$10^{4}-5\times10^{4}$	Sensitive to Li

[a] The range expressions in this row are all represented as "laboratory – synchrotron." The cost of synchrotron X-ray tomography is extremely high because of the construction and maintenance of synchrotron facilities.

[b] Neutron tomography can achieve 3D imaging at the expense of the temporal resolution. The cost of neutron imaging is extremely high because of the construction and maintenance of neutron facilities.

Application of PAM in batteries

PAM for Li metal

Our group demonstrated that PAM can be used for Li-metal battery imaging, with high-quality images of Li dendrites obtained [19]. A home-built PAM system was used to image the Li metal in Li/Li symmetric cells [19]. The lateral resolution of this system was 3.3 μm, and the axial resolution was 26 μm. A glass-fiber separator soaked with liquid electrolyte was sandwiched between two Li-metal electrodes. As shown in Fig. 4(a), the battery was cut, and a flat cross section was exposed for PAM measurement. The pulsed laser was focused on the cross section; meanwhile, a hydrophone was placed above the sample to collect the photoacoustic signals. By lateral scanning of the sample, 3D PAM images can be obtained. To ensure that there was no air between the sample and the hydrophone, the sample was sealed in a transparent bag filled with liquid electrolyte. Through experiments, the threshold of laser energy at which the sample would not be damaged was estimated. Accordingly, the laser energy used in this work was ~ 86 nJ.

The PAM and OM results were first compared. Figure 4(b) presents the PAM image of a selected area of the cross section. The same area was observed using OM by marking the sample beforehand, and Fig. 4(c) shows the corresponding OM image. For a clearer view, the regions within the dotted boxes in Figs. 4(b) and (c) were enlarged and are presented in Figs. 4(d) and (e), respectively. In the PAM images, there are two distinct areas. The area consisting of red pixels represents a material with strong photoacoustic signals (from Li metal or the marker), whereas the other area consisting of black pixels indicates a material with almost no photoacoustic signals (e.g., corresponding to the separator). In the OM images, the positions of Li metal and the separator can be confirmed although with relatively low contrast. In the PAM images, it can be observed good correspondence of the Li metal area and the separator area with the OM images. These results suggest that PAM is a reliable imaging technology for Li metal. Further, the much clearer boundary

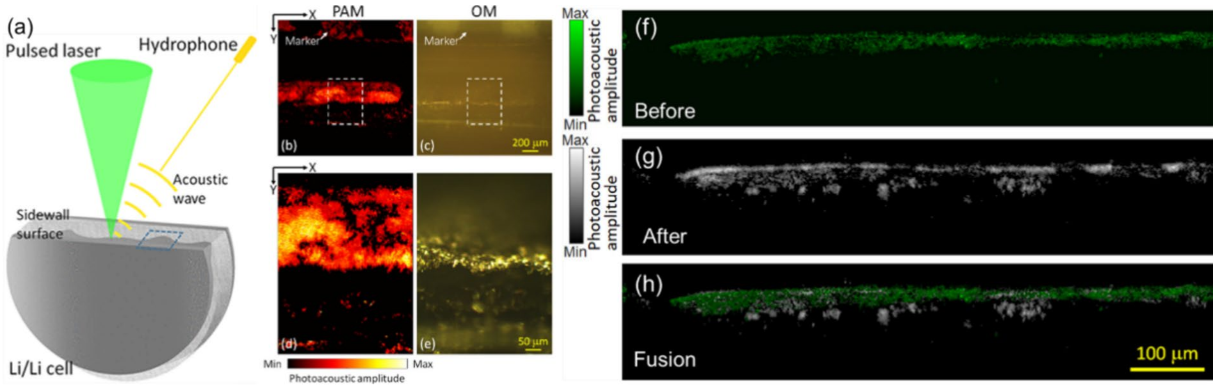

Figure 4: PAM of cross section of a Li/Li symmetric cell. (a) Schematic of imaging of the cross section of a Li/Li symmetric cell. (b) PAM image of a Li/Li symmetric cell. (c) Corresponding OM image of (b). (d) PAM image of the region in the dashed box in (b). (e) OM image of the region in the dashed box in (c). (f) PAM image of Li-metal anode before charging. (g) PAM image of Li-metal anode after charging. (h) PAM image obtained by laying (f) on (g). Reprinted with permission for Ref. [19], Copyright 2020 American Chemical Society.

between Li metal and the separator in the PAM images indicates that the contrast of PAM is significantly better than that of OM.

The deposition heterogeneity of Li metal can also be clearly captured by PAM of Li-metal batteries. The morphology of a pristine Li anode (cross section) in a Li/Li symmetric cell was captured by PAM, as shown in Fig. 4(f). Then, the Li/Li symmetric cell was assembled in coin-cell cases and was charged for 15 h under a current density of 1 mA/cm^2. Figure 4(g) presents an image of the Li-metal anode captured after being charged. Figure 4(h) shows the fusion figure, where the two PAM cross-sectional images of the cell before and after charging [Figs. 4(f) and (g)] are overlapped. In Fig. 4(h), the differences between Figs. 4(f) and (g) can be distinguished. The Li-metal anode before charging was relatively flat. In contrast, irregular Li protrusions were detected after charging, confirming the inhomogeneous deposition of Li on the anode.

Another experiment was also extended to cells with different deposition thicknesses of Li metal (the thickness can be controlled by electrochemistry). Because of the high contrast between Li metal and the separator, the thickness of the Li-metal anode can be directly calculated from PAM images, and the results qualitatively agree with electrochemistry data.

Aiming to achieve improved quantitative analysis, PAM for top-view imaging was developed [33]. The PAM system was primarily the same as the system for cross-sectional imaging and had similar lateral and axial resolution. Top-view imaging of the cells using Li metal as the anode and a copper pellet as the counter electrode (Li/Cu cell) was conducted. To image such cells, there was no need to cut out the cross section, and thus, the integrity of the cells was maintained. The reason for selecting copper electrodes is that they are harder and less prone to deform after a pressurized package than Li electrodes. Before experiments, copper pellets were polished by sandpaper to obtain smooth substrates, which are essential for PAM to produce good images. Five Li/Cu cells were discharged with different areal capacities varying from 2 to 10 mAh/cm^2 for quantitative study. During discharging, Li metal is deposited on the copper electrodes. The copper electrodes were then carefully taken from the cells for PAM imaging. Figure 5 shows the imaging results. For Fig. 5(a) – (t), each column corresponds to a discharging areal capacity. Figure 5(a)–(e) (the first row) shows photoacoustic MAP images of the Li-deposited copper electrodes. Using an image processing algorithm [33], the regions with and without Li depositions can be segmented, as shown in Fig. 5(k)–(o) (the third row) and Fig. 5(f)–(j) (the second row), respectively, which are photoacoustic height-encoded images representing the deposited Li height (for the region with Li depositions) and copper height (for the region without Li depositions), respectively. Note that Fig. 5(f)–(j) is utilized to estimate the original copper surface (i.e., before Li depositions) by a second-order polynomial fit. Finally, the thickness of electrochemically deposited Li can be calculated by subtracting the estimated original copper surface from the deposited Li height in Fig. 5(k)–(o). The deposited Li thickness is shown in Fig. 5(p)–(t) (the fourth row).

The masses of deposited Li can be calculated from the thickness, as indicated by the red points in Fig. 5(u), by converting the thickness to volume and assuming the theoretical density of Li metal. The black line shows the theoretical masses calculated using electrochemistry curves. There is a great consistency between the masses calculated from the electrochemistry curves and the masses calculated using PAM, although the

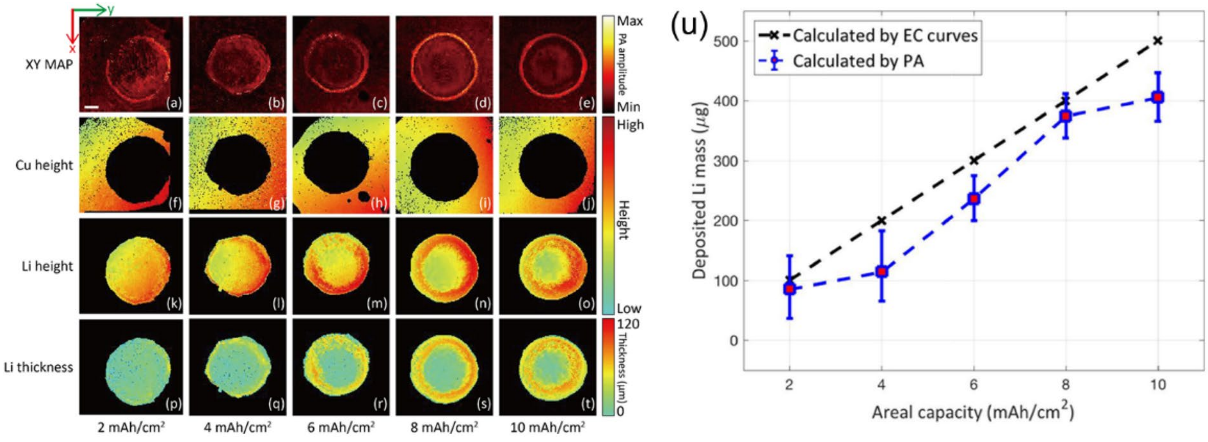

Figure 5: Top-view PAM imaging of deposited Li on the copper electrodes for quantitative analysis. (a)–(e) Photoacoustic MAP images of the Li-deposited copper electrodes. (f)–(j) Photoacoustic height-encoded images of the copper height for the region without Li depositions. (k)–(o) Photoacoustic height-encoded images of the deposited Li height for the region with Li depositions. (p)–(t) Thickness images of electrochemically deposited Li. PA: photoacoustic. The scale bar in the figures is 1 mm. (u) Comparison of theoretical results calculated using electrochemistry curves and estimated results using PAM images. Reprinted from Ref. [33], Copyright 2020 Society of Photo-Optical Instrumentation Engineers (SPIE).

photoacoustic results are always smaller than the electrochemistry results. Part of the reason for this discrepancy is that the axial resolution of the system was low, causing a calculation error. To overcome this problem, a dual-view PAM system may be a good choice [46]. Another reason is the Li loss when isolating the copper electrodes from the cells. A new separator material that the laser can penetrate through may be beneficial because it would enable photoacoustic imaging without the removal of the separator. Finally, the hydrophone was simply assumed to be placed along the axial direction, and the oblique angle of the hydrophone was not considered [Fig. 4(a)]. The obliquely placed hydrophone would underestimate the height difference of the deposited Li height and copper height compared with a hydrophone placed along the axial direction, which leads to an underestimated thickness of the deposited Li and thus smaller masses.

3D spatial distribution of Li metal can also be obtained using PAM. When combined with other methods such as gas chromatography and electrochemical impedance spectroscopy, PAM can be used to quantitatively study freshly deposited Li and "dead" Li [20]. In the preceding paragraph, we discussed the imaging of freshly deposited Li with a capacity of 10 mAh/cm^2. More detailed quantitative analysis was performed in [20], and the results are shown in Fig. 6. According to the capacity loss tendency analysis in the work [20], the remained capacity approached 10 mAh/cm^2 after 45 cycles. Hence, the accumulative "dead" Li on the copper surface after 45 cycles was imaged by PAM. In this case, a freshly deposited Li-metal surface and the accumulative "dead" Li-metal surface with a similar capacity were compared. The average height of the freshly deposited Li was approximately 44.35 μm and that of the accumulative "dead" Li was approximately 39.76 μm, which are comparable. The height distributions of these two different states of Li-metal surfaces are presented in Fig. 6(d). As observed, the variance of the accumulative "dead" Li was much larger than that of the freshly deposited Li. Such quantitative analysis of lithium morphology is important for the study of battery failure mechanisms.

PAM can be applied to all-solid-state Li-metal batteries. In a short circuit, all-solid-state cell with $LiNi_{0.5}Co_{0.2}Mn_{0.3}O_2$ (NMC532) as the cathode, Li metal as the anode, and a polyethylene oxide (PEO) film as the electrolyte, the 3D structure of a Li dendrite inside the cell was reconstructed using PAM imaging, as illustrated in Fig. 7(a). In addition, PAM imaging was conducted on ceramic–polymer composite solid electrolytes. Figure 7(b) and (c) presents the 2D and 3D results, respectively. The area with the strong photoacoustic amplitude is attributed to solid-electrolyte fillers, and the area without photoacoustic amplitude represents the PEO polymer. This approach potentially allows us to follow the morphology and porosity changes for different processing conditions, establishing crucial links between processing, microstructure, and electrochemical performance of the solid-state electrolyte. Such understanding is relatively lacking in the battery community.

Recently, PAM has advanced toward non-contact imaging. Conventionally, PAM systems detect the ultrasound signals that propagate outward from the light-absorbing material of a sample. In this case, the ultrasound propagation path must be filled with liquid or solid, as an ultrasonic coupling medium, to facilitate acoustic coupling. The ultrasonic coupling medium is in direct contact with the sample. If the contact is unstable or imperfect, the image quality will be greatly impaired. Moreover, sample preparation and imaging procedure can be complicated and challenging for selected applications. This type of conventional PAM using an ultrasonic coupling medium is called

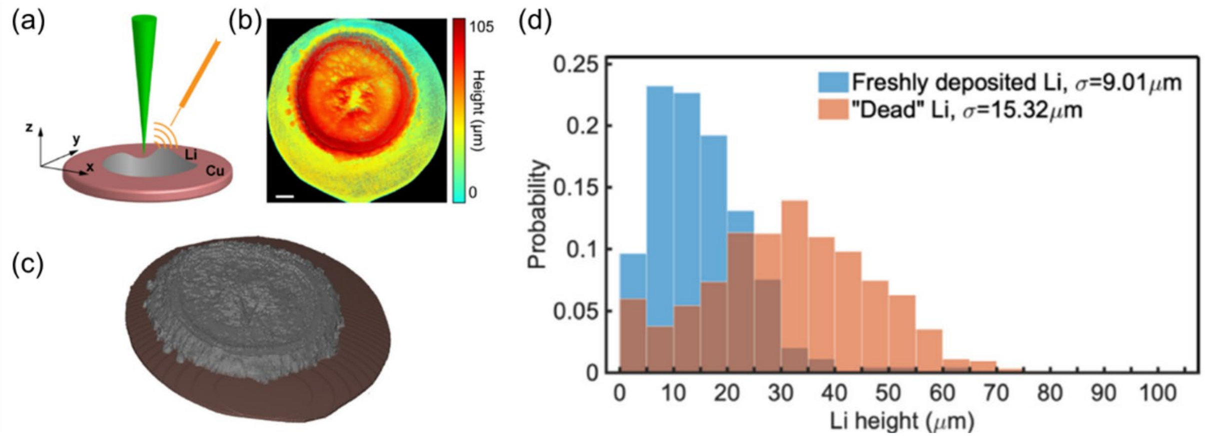

Figure 6: 3D spatial distribution of Li metal. (a) Schematic of top-view PAM imaging of deposited Li on copper electrodes. (b) Photoacoustic depth-encoded images of "dead" Li with a capacity density of 10 mAh/cm^2. The scale bar in the figures is 1 mm. (c) 3D rendering of height distribution of (b). (d) Comparison of height distributions of freshly deposited Li and "dead" Li. Reprinted with permission from Ref. [20], Copyright 2021 American Chemical Society.

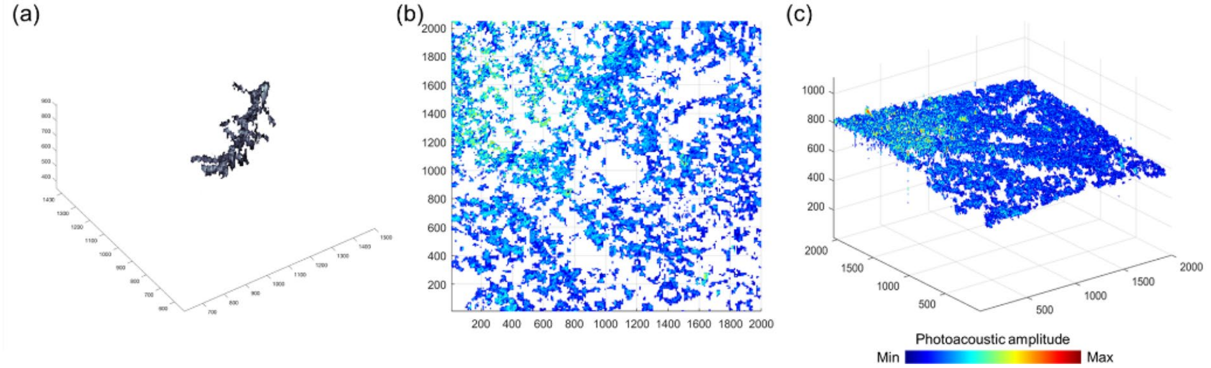

Figure 7: Application of PAM in the solid-state electrolyte. (a) 3D structure of Li dendrite in the PEO electrolyte. (b) Photoacoustic MAP image of the composite solid electrolyte in the *x*–*y* plane. (c) 3D rendering of photoacoustic image of the composite solid electrolyte. The units in the figures are µm.

contact PAM [47]. In contrast, photoacoustic remote sensing (PARS) microscopy is a promising non-contact PAM technique, first established by HajiReza et al. in 2017 [48]. In PARS microscopy, there are two light beams with different wavelengths. One of them is the photoacoustic excitation laser, which illuminates the sample and produces acoustic waves via the photoacoustic effect. Instead of detecting ultrasound waves, the other interrogation light beam is used to retrieve the refractive-index change caused by the initial acoustic pressure induced in the sample. In this way, acoustic coupling media are no longer needed, which enables non-contact imaging. Recently, PARS microscopy was applied to successfully visualize Li dendrites [49]. The specific configuration of PARS microscopy is shown in Fig. 8(a). In this system, a 1064 nm laser worked as the excitation light beam, and a 1310 nm laser served as the interrogation light beam. The light path of the excitation laser was similar to that in conventional PAM. The interrogation laser was combined with the excitation laser using a wavelength division multiplexer (WDM). The lateral resolution of the PARS microscopy setup was measured to be 2–5 µm, and the axial resolution was only ~ 123 µm. The cross sections of Li/Li symmetric cells were imaged, similar to Fig. 4(b) and (d). A smooth electrode without Li depositions is shown in Fig. 8(c), where the width of the red region (representing Li) is ~ 240 µm, which is consistent with the thickness of the Li foil. Figure 8(d) shows the morphology of the deposited Li on the electrode at a current density of 1 mA/cm^2 for 15 h, and obvious Li protrusions can be observed. This work reveals the great potential of PARS microscopy in batteries, especially for all-solid-state batteries where no liquid is present.

PAM for electrode properties

Strong photoacoustic signals can also be received from typical cathode materials in Li-ion batteries, which can be used to measure the porosity and tortuosity of the cathode, detect the degree of wetting in the battery, and track the evolution of the cathode structure. As an example, strong photoacoustic signals were detected from NMC532, a cathode material, allowing photoacoustic imaging of NMC532, as shown in Fig. 9(a). However, there is no photoacoustic signal at some points of the NMC532 sample, which may indicate pores on the cathode. The results suggest that PAM is a promising method for porosity and tortuosity measurement to replace mercury intrusion. It is also possible to track structural changes according to the 3D rendering image in Fig. 9(b), which may be helpful to reveal the mechanism behind the structural changes as well as the relationship between the cathode structure and failure of batteries. As previously mentioned, the photoacoustic signal will be significantly attenuated if liquid is lacking. Using this property, the degree of wetting can also be measured by PAM, which is an important parameter related to the failure of batteries.

Other than cathode materials, a graphite anode can also be studied by PAM. A graphite anode was extracted from an operated cell and cut to expose the flat cross section. The sample was sealed in a transparent bag made of polyethylene and was filled with liquid electrolyte for PAM imaging. Figure 10(a) and (b) shows the PAM images of the graphite anode. The white arrows indicate protrusions on the graphite surface, which are most likely Li metal formed by the reduction of Li ions not intercalated into the graphite anode. The results indicate that PAM can also be applied to analyze Li dendrites on a graphite surface. In addition, the strong photoacoustic signals from graphite enable monitoring of the changes in the graphite electrode itself during cycling.

Future perspectives

Current PAM for batteries still needs improvement. First, although PAM meets the basic requirements for in operando experiments, there is no mature method for in operando sample preparation at present. Secondly, the spatial resolution of

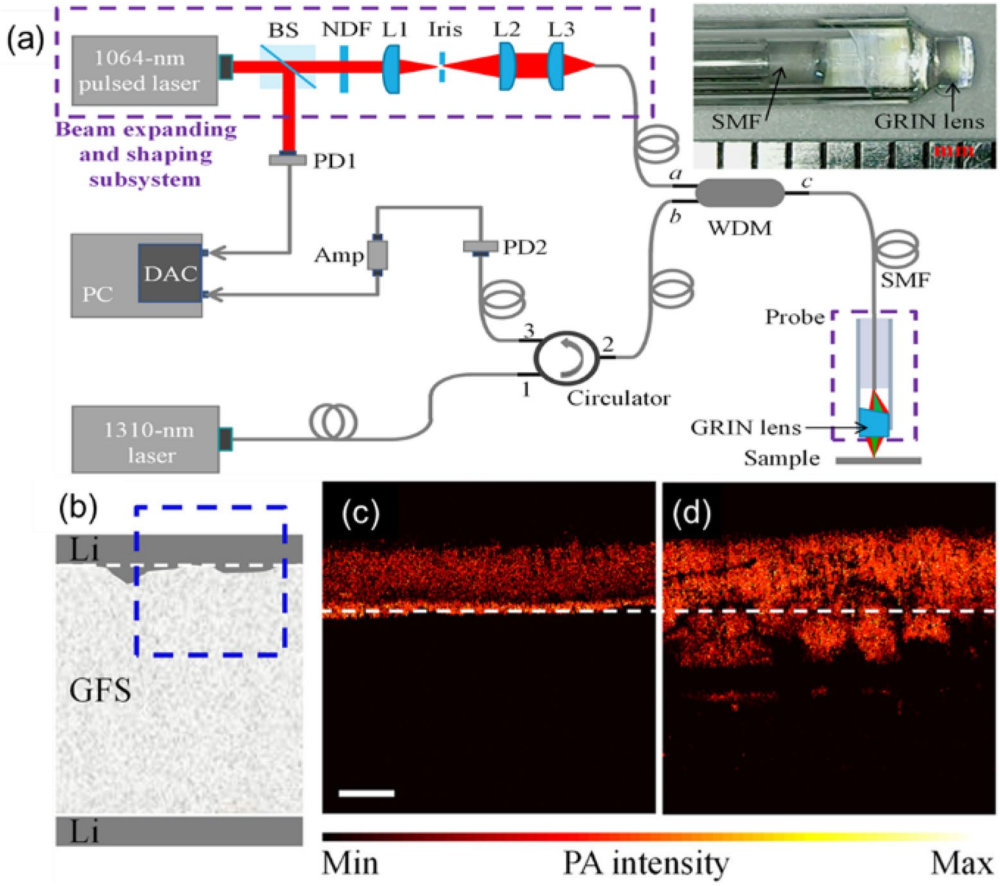

Figure 8: PARS microscopy for batteries. (a) Configuration of PARS microscopy. BS: beam splitter; NDF: neutral density filter; PD1 and PD2: photodetectors; DAC: data acquisition card; PC: personal computer; Amp: preamplifier; L1, L2, and L3: lens; WDM: wavelength division multiplexer; SMF: single-mode fiber. (Upper-right picture: miniature probe with a diameter of ~ 3.0 mm). (b) Sketch of the sample with sandwich structure. The region in the blue dashed box was imaged. (c) Photoacoustic MAP image from the cell sample without charging. (d) Photoacoustic MAP image from the cell sample after charging. PA: photoacoustic. The scale bar in the figures is 200 μm. Reprinted from Ref. [49], Copyright © 2021 Optica Publishing Group.

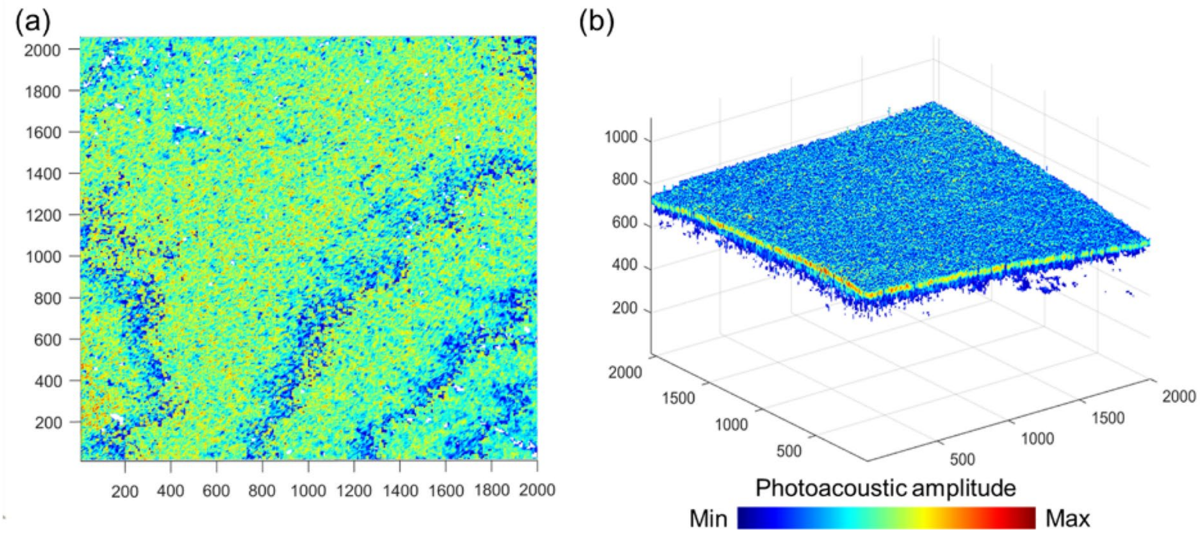

Figure 9: Application of PAM in a cathode. (a) Photoacoustic MAP image of NMC532 in the x–y plane. (b) 3D rendering of photoacoustic image of NMC532. The units in the figures are μm.

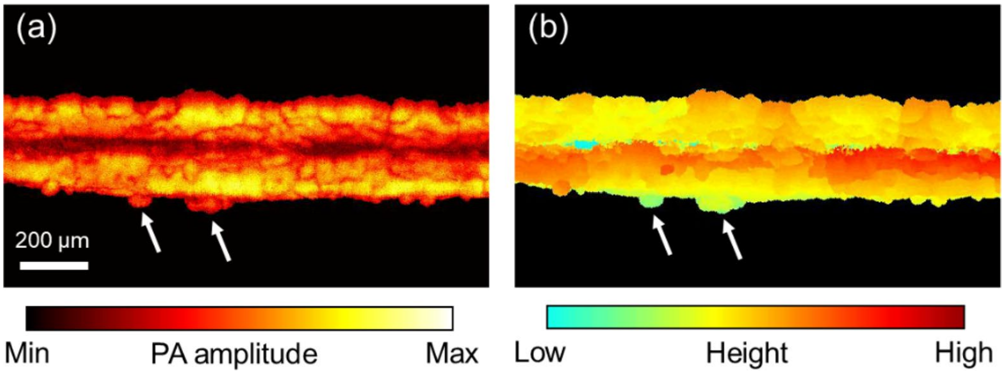

Figure 10: Application of PAM in a graphite anode. (a) Photoacoustic MAP image of graphite anode. (b) Photoacoustic height-encoded image of graphite anode. PA: photoacoustic

the PAM system used in battery imaging still has room for further improvement, especially the axial resolution. The system currently in use has lateral and axial resolutions of 3.3 and 26 μm, respectively [19], which are far from the highest spatial resolution that a PAM system can achieve (lateral resolution of 200 nm [43] and axial resolution of 5.8 μm [45]). Finally, PAM is only used for morphology observation now. However, PAM has the potential to be used for porosity determination and the degree of electrolyte wetting detection, which require more attempts and in-depth data analysis. Additional information can be also obtained by a dual-model system combining PAM with another imaging or spectroscopy method (such as fluorescence or Raman).

In situ and in operando experiments

The nondestructive nature and relatively high temporal resolution of PAM indicate the possibility of conducting in situ experiments. The greatest difficulty may be designing a battery structure with an optically transparent and acoustically transparent window. In PAM, acoustic transparency typically requires a thin, and soft material. In other words, visually transparent, thin and soft electrodes and separators are needed. Besides, the in situ samples had better be close to the real battery state. Therefore, in situ PAM for batteries requires innovations in electrode and separator materials as well as a suitable design of the battery structure, which are challenging.

For in operando experiments, a PAM system with higher imaging speed is imperative. If an image with a large scale (field of view) and high spatial resolution is desired, the image will contain many pixels. Especially for a sample with weak photoacoustic signals (i.e., low SNR), signal averaging may be applied by repeated scanning, which will worsen the temporal resolution. For the PAM system using the motorized stage, the scanning speed is limited by the acceleration and deceleration of the motor. State-of-the-art PAM systems adopt a microelectromechanical system (MEMS) mirror to enhance the scanning speed. Briefly, the excitation laser spot is raster scanned on the sample by the MEMS mirror, and fast scanning can be realized by virtue of the fast response of the MEMS mirror. As an example, considering 256 × 256 pixels and a laser with a pulse repetition frequency of 1 kHz, the shortest scanning time of ~ 66 s can be achieved using the MEMS mirror, which is approximately five times faster than the system shown in Fig. 3(a). With a laser with higher pulse repetition frequency, the scanning time can be further shortened. Such a fast scanning speed can support not only in operando experiments but also large-scale scanning for analysis of the entire sample. If a high temporal resolution is not essential, repeated scanning can be used to enhance the SNR by signal averaging.

Dual-view PAM and dual-modal system

Multi-view imaging can be used to obtain sample information from different angles to achieve higher resolution and more accurate images [50]. Multi-view imaging implemented in OR-PAM has been demonstrated, and a lateral resolution of 2.0 μm and an axial resolution of 4.7 μm were achieved [51]. Notably, the axial resolution was greatly enhanced compared with that of the single-view counterpart. Another dual-view OR-PAM system was built using ultraviolet wavelength for photoacoustic excitation, which had a resolution of 1.8, 1.3, and 1.8 μm along the *x*, *y*, and *z* directions, respectively [46], and quantitative imaging of cell nuclei was demonstrated. The improved spatial resolution of multi-view or dual-view OR-PAM systems is highly desirable for accurate quantification and analysis of batteries.

When PAM cannot fully meet the research requirements, combining PAM with another imaging technology can be a good solution. For instance, the incorporation of optical coherence tomography may provide layered information in batteries [52]. In addition, the integration of fluorescence imaging together with the use of suitable fluorescent dyes or

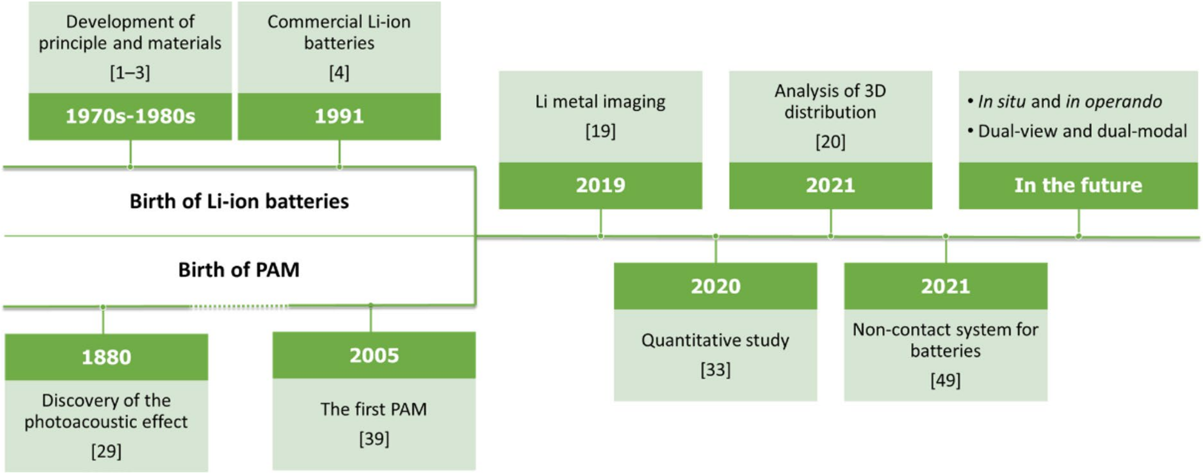

Figure 11: Historical development of batteries and PAM, and future research directions of PAM imaging of batteries

probes may provide good sensitivity as a complement when detecting hydrogen sulfide [53]. Our group demonstrated a novel system combining non-contact PAM and fluorescence microscopy, which can facilitate cell imaging and ophthalmic imaging [54]. The system is expected to be useful for battery imaging as well. The progressive dual-modal system may accelerate research on batteries.

Conclusion

In conclusion, PAM is a nondestructive imaging method that provides high speed, 3D imaging, good spatial resolution, and satisfactory contrast. Recently, PAM has been increasingly used in batteries (Fig. 11). The successful acquisition of high-quality Li-metal images using PAM has demonstrated that PAM is an effective imaging method for batteries. Furthermore, quantitative results and 3D spatial distributions from PAM have been used to analyze Li metal in different states, with the results indicating that the distribution of accumulative "dead" Li was more inhomogeneous. This type of quantitative analysis is particularly helpful for understanding battery failure mechanisms. Recently, non-contact PAM for batteries has been explored, which can facilitate the study of all-solid-state batteries. In the future, PAM for battery imaging may be developed in several aspects such as in situ imaging, *in operando* imaging, dual-view OR-PAM systems, and dual-modal PAM systems.

Acknowledgments

This work was supported by National Key R&D program of China (Contract No. 2021YFB3800300) and Natural Science Foundation of Shanghai (Contract No. 22ZR1428900).

Data availability

Some data analyzed during this study are included in the published articles, others are available from the corresponding author on reasonable request.

Declarations

Conflict of interest On behalf of all authors, the corresponding authors state that there is no conflict of interest.

References

1. M.S. Whittingham, Electrical energy storage and intercalation chemistry. Science **192**, 1126–1127 (1976). https://doi.org/10.1126/science.192.4244.1126
2. K. Mizushima, P.C. Jones, P.J. Wiseman, J.B. Goodenough, $LixCoO_2$ ($0 < x \leq 1$): A new cathode material for batteries of high energy density. Mater. Res. Bull. **15**, 783–789 (1980). https://doi.org/10.1016/0025-5408(80)90012-4
3. A. Yoshino, K. Sanechika, T. Nakajima, Secondary battery (1987)
4. A. Yoshino, The birth of the lithium-ion battery. Angew. Chem. Int. Ed. **51**, 5798–5800 (2012). https://doi.org/10.1002/anie.201105006
5. J.B. Goodenough, K.-S. Park, The Li-ion rechargeable battery: a perspective. J. Am. Chem. Soc. **135**, 1167–1176 (2013). https://doi.org/10.1021/ja3091438
6. C.-X. Zu, H. Li, Thermodynamic analysis on energy densities of batteries. Energy Environ. Sci. **4**, 2614 (2011). https://doi.org/10.1039/c0ee00777c
7. X.-B. Cheng, R. Zhang, C.-Z. Zhao, Q. Zhang, Toward safe lithium metal anode in rechargeable batteries: a review. Chem. Rev. **117**, 10403–10473 (2017). https://doi.org/10.1021/acs.chemrev.7b00115

8. A. Manthiram, A reflection on lithium-ion battery cathode chemistry. Nat. Commun. **11**, 1550 (2020). https://doi.org/10.1038/s41467-020-15355-0
9. M.J. Loveridge, G. Remy, N. Kourra, R. Genieser, A. Barai, M.J. Lain, Y. Guo, M. Amor-Segan, M.A. Williams, T. Amietszajew, M. Ellis, R. Bhagat, D. Greenwood, Looking deeper into the galaxy (Note 7). Batteries **4**, 3 (2018). https://doi.org/10.3390/batteries4010003
10. K. Liu, Y. Liu, D. Lin, A. Pei, Y. Cui, Materials for lithium-ion battery safety. Sci. Adv. (2018). https://doi.org/10.1126/sciadv.aas9820
11. Y. Xu, H. Zheng, H. Yang, Y. Yu, J. Luo, T. Li, W. Li, Y.-N. Zhang, Y. Kang, Thermodynamic regulation of dendrite-free Li plating on Li_3Bi for stable lithium metal batteries. Nano Lett. **21**, 8664–8670 (2021). https://doi.org/10.1021/acs.nanolett.1c02613
12. Z. Li, M. Peng, X. Zhou, K. Shin, S. Tunmee, X. Zhang, C. Xie, H. Saitoh, Y. Zheng, Z. Zhou, Y. Tang, In situ chemical lithiation transforms diamond-like carbon into an ultrastrong ion conductor for dendrite-free lithium-metal anodes. Adv. Mater. **33**, 2100793 (2021). https://doi.org/10.1002/adma.202100793
13. P. Bai, J. Li, F. Brushett, M. Bazant, Transition of lithium growth mechanisms in liquid electrolytes. Energy Environ. Sci. **9**, 3221–3229 (2016). https://doi.org/10.1039/C6EE01674J
14. N.B. Aetukuri, S. Kitajima, E. Jung, L.E. Thompson, K. Virwani, M.-L. Reich, M. Kunze, M. Schneider, W. Schmidbauer, W.W. Wilcke, D.S. Bethune, J.C. Scott, R.D. Miller, H.-C. Kim, Flexible ion-conducting composite membranes for lithium batteries. Adv. Energy Mater. **5**, 1500265 (2015). https://doi.org/10.1002/aenm.201500265
15. X. Fu, R. Odstrcil, M. Qiu, J. Liu, W.-H. Zhong, Natural "relief" for lithium dendrites: tailoring protein configurations for long-life lithium metal anodes. Energy Storage Mater. **42**, 22–33 (2021). https://doi.org/10.1016/j.ensm.2021.07.010
16. X. Zhang, F. Ma, K. Srinivas, B. Yu, X. Chen, B. Wang, X. Wang, D. Liu, Z. Zhang, J. He, Y. Chen, Fe3N@N-doped graphene as a lithiophilic interlayer for highly stable lithium metal batteries. Energy Storage Mater. **45**, 656–666 (2022). https://doi.org/10.1016/j.ensm.2021.12.010
17. D. Cao, X. Sun, Q. Li, A. Natan, P. Xiang, H. Zhu, Lithium dendrite in all-solid-state batteries: growth mechanisms, suppression strategies, and characterizations. Matter **3**, 57–94 (2020). https://doi.org/10.1016/j.matt.2020.03.015
18. H. Pan, T. Fu, G. Zan, R. Chen, C. Yao, Q. Li, P. Pianetta, K. Zhang, Y. Liu, X. Yu, H. Li, Fast Li plating behavior probed by X-ray computed tomography. Nano Lett. **21**, 5254–5261 (2021). https://doi.org/10.1021/acs.nanolett.1c01389
19. H. Liu, Y. Zhao, J. Zhou, P. Li, S.-H. Bo, S.-L. Chen, Photoacoustic imaging of lithium metal batteries. ACS Appl. Energy Mater. **3**, 1260–1264 (2020). https://doi.org/10.1021/acsaem.9b01791
20. Y. Zhao, Y. Wu, H. Liu, S.L. Chen, S.H. Bo, Accelerated growth of electrically isolated lithium metal during battery cycling. ACS Appl. Mater. Interfaces **13**, 35750–35758 (2021). https://doi.org/10.1021/acsami.1c08944
21. L. Froboese, P. Titscher, B. Westphal, W. Haselrieder, A. Kwade, Mercury intrusion for ion- and conversion-based battery electrodes—structure and diffusion coefficient determination. Mater. Charact. **133**, 102–111 (2017). https://doi.org/10.1016/j.matchar.2017.09.002
22. Z. Deng, Z. Huang, L. Liu, Y. Huang, Y. Shen, Applications of ultrasound technique in characterization of lithium-ion batteries. Energy Storage Sci. Technol. **8**, 1033–1039 (2019). https://doi.org/10.12028/j.issn.2095-4239.2019.0146
23. Z. Deng, Z. Huang, Y. Shen, Y. Huang, H. Ding, A. Luscombe, M. Johnson, J.E. Harlow, R. Gauthier, J.R. Dahn, Ultrasonic scanning to observe wetting and "unwetting" in Li-ion pouch cells. Joule **4**, 2017–2029 (2020). https://doi.org/10.1016/j.joule.2020.07.014
24. W.J. Weydanz, H. Reisenweber, A. Gottschalk, M. Schulz, T. Knoche, G. Reinhart, M. Masuch, J. Franke, R. Gilles, Visualization of electrolyte filling process and influence of vacuum during filling for hard case prismatic lithium ion cells by neutron imaging to optimize the production process. J. Power Sources **380**, 126–134 (2018). https://doi.org/10.1016/j.jpowsour.2018.01.081
25. J. Janek, W.G. Zeier, A solid future for battery development. Nat. Energy **1**, 16141 (2016). https://doi.org/10.1038/nenergy.2016.141
26. Z. Ning, D.S. Jolly, G. Li, R. De Meyere, S.D. Pu, Y. Chen, J. Kasemchainan, J. Ihli, C. Gong, B. Liu, D.L.R. Melvin, A. Bonnin, O. Magdysyuk, P. Adamson, G.O. Hartley, C.W. Monroe, T.J. Marrow, P.G. Bruce, Visualizing plating-induced cracking in lithium-anode solid-electrolyte cells. Nat. Mater. **20**, 1121–1129 (2021). https://doi.org/10.1038/s41563-021-00967-8
27. S. Luo, Z. Wang, X. Li, X. Liu, H. Wang, W. Ma, L. Zhang, L. Zhu, X. Zhang, Growth of lithium–indium dendrites in all-solid-state lithium-based batteries with sulfide electrolytes. Nat. Commun. **12**, 1–10 (2021). https://doi.org/10.1038/s41467-021-27311-7
28. L. Ye, X. Li, A dynamic stability design strategy for lithium metal solid state batteries. Nature **593**, 218–222 (2021). https://doi.org/10.1038/s41586-021-03486-3
29. A.G. Bell, On the production and reproduction of sound by light. Am. J. Sci. **20**, 305–324 (1880). https://doi.org/10.2475/ajs.s3-20.118.305
30. M. Seong, S.-L. Chen, Recent advances toward clinical applications of photoacoustic microscopy: a review. Sci. China Life Sci. **63**, 1798–1812 (2020). https://doi.org/10.1007/s11427-019-1628-7
31. S. Jeon, J. Kim, D. Lee, J.W. Baik, C. Kim, Review on practical photoacoustic microscopy. Photoacoustics **15**, 100141 (2019). https://doi.org/10.1016/j.pacs.2019.100141
32. L.V. Wang, Tutorial on photoacoustic microscopy and computed tomography. IEEE J. Sel. Top. Quantum Electron. **14**, 171–179 (2008). https://doi.org/10.1109/JSTQE.2007.913398
33. H. Liu, Y. Zhao, S.-H. Bo, S.-L. Chen, Application of photoacoustic imaging for lithium metal batteries. Adv. Opt. Imaging Technol. **11549**, 90 (2020)

34. V.T. Nguyen, N.T.P. Truong, V.H. Pham, J. Choi, S. Park, C.D. Ly, S.-W. Cho, S. Mondal, H.G. Lim, C.-S. Kim, J. Oh, Ultra-wide-field photoacoustic microscopy with a dual-channel slider-crank laser-scanning apparatus for in vivo biomedical study. Photoacoustics **23**, 100274 (2021). https://doi.org/10.1016/j.pacs.2021.100274
35. T. Jin, H. Guo, H. Jiang, B. Ke, L. Xi, Portable optical resolution photoacoustic microscopy (pORPAM) for human oral imaging. Opt. Lett. **42**, 4434–4437 (2017). https://doi.org/10.1364/OL.42.004434
36. H.F. Zhang, K. Maslov, G. Stoica, L.V. Wang, Functional photoacoustic microscopy for high-resolution and noninvasive in vivo imaging. Nat. Biotechnol. **24**, 848–851 (2006). https://doi.org/10.1038/nbt1220
37. X. Shu, H. Li, B. Dong, C. Sun, H.F. Zhang, Quantifying melanin concentration in retinal pigment epithelium using broadband photoacoustic microscopy. Biomed. Opt. Express. **8**, 2851–2865 (2017). https://doi.org/10.1364/BOE.8.002851
38. L.V. Wang, S. Hu, Photoacoustic tomography. In vivo imaging from organelles to organs. Science **335**, 1458–1462 (2012). https://doi.org/10.1126/science.1216210
39. K. Maslov, G. Stoica, L.V. Wang, In vivo dark-field reflection-mode photoacoustic microscopy. Opt. Lett. **30**, 625 (2005). https://doi.org/10.1364/OL.30.000625
40. L. Song, K.I. Maslov, R. Bitton, K.K. Shung, L.V. Wang, Fast 3-D dark-field reflection-mode photoacoustic microscopy in vivo with a 30-MHz ultrasound linear array. J. Biomed. Opt. **13**, 054028 (2008). https://doi.org/10.1117/1.2976141
41. K. Maslov, H.F. Zhang, S. Hu, L.V. Wang, Optical-resolution photoacoustic microscopy for in vivo imaging of single capillaries. Opt. Lett. **33**, 929 (2008). https://doi.org/10.1364/OL.33.000929
42. D.-K. Yao, K. Maslov, K.K. Shung, Q. Zhou, L.V. Wang, In vivo label-free photoacoustic microscopy of cell nuclei by excitation of DNA and RNA. Opt. Lett. **35**, 4139 (2010). https://doi.org/10.1364/OL.35.004139
43. C. Zhang, K. Maslov, L.V. Wang, Subwavelength-resolution label-free photoacoustic microscopy of optical absorption in vivo. Opt. Lett. **35**, 3195 (2010). https://doi.org/10.1364/OL.35.003195
44. C. Zhang, K.I. Maslov, J. Yao, L.V. Wang, In vivo photoacoustic microscopy with 7.6-μm axial resolution using a commercial 125-MHz ultrasonic transducer. J. Biomed. Opt. **17**, 116016 (2012). https://doi.org/10.1117/1.JBO.17.11.116016
45. C. Zhang, Y. Zhou, C. Li, L.V. Wang, Slow-sound photoacoustic microscopy. Appl. Phys. Lett. **102**, 163702 (2013). https://doi.org/10.1063/1.4803444
46. D. Cai, T.T.W. Wong, L. Zhu, J. Shi, S.-L. Chen, L.V. Wang, Dual-view photoacoustic microscopy for quantitative cell nuclear imaging. Opt. Lett. **43**, 4875–4878 (2018). https://doi.org/10.1364/OL.43.004875
47. Z. Hosseinaee, M. Le, K. Bell, P.H. Reza, Towards non-contact photoacoustic imaging [review]. Photoacoustics **20**, 100207 (2020). https://doi.org/10.1016/j.pacs.2020.100207
48. P. Hajireza, W. Shi, K. Bell, R.J. Paproski, R.J. Zemp, Non-interferometric photoacoustic remote sensing microscopy. Light Sci. Appl. **6**, e16278–e16278 (2017). https://doi.org/10.1038/lsa.2016.278
49. J. Zhou, J. Zhou, W. Wang, S. Liang, L. Jing, S.-H. Bo, S.-L. Chen, Miniature non-contact photoacoustic probe based on fiber-optic photoacoustic remote sensing microscopy. Opt. Lett. **46**, 5767 (2021). https://doi.org/10.1364/OL.444889
50. Y. Wu, X. Han, Y. Su, M. Glidewell, J.S. Daniels, J. Liu, T. Sengupta, I. Rey-Suarez, R. Fischer, A. Patel, C. Combs, J. Sun, X. Wu, R. Christensen, C. Smith, L. Bao, Y. Sun, L.H. Duncan, J. Chen, Y. Pommier, Y.-B. Shi, E. Murphy, S. Roy, A. Upadhyaya, D. Colón-Ramos, P. La Riviere, H. Shroff, Multiview confocal super-resolution microscopy. Nature **600**, 279–284 (2021). https://doi.org/10.1038/s41586-021-04110-0
51. L. Zhu, L. Li, L. Gao, L.V. Wang, Multiview optical resolution photoacoustic microscopy. Optica **1**, 217–222 (2014). https://doi.org/10.1364/OPTICA.1.000217
52. X. Zhu, Z. Huang, Z. Li, W. Li, X. Liu, Z. Chen, J. Tian, C. Li, Resolution-matched reflection mode photoacoustic microscopy and optical coherence tomography dual modality system. Photoacoustics **19**, 100188 (2020). https://doi.org/10.1016/j.pacs.2020.100188
53. Z. Chen, X. Mu, Z. Han, S. Yang, C. Zhang, Z. Guo, Y. Bai, W. He, An optical/photoacoustic dual-modality probe: ratiometric in/ex vivo imaging for stimulated H_2S upregulation in mice. J. Am. Chem. Soc. **141**, 17973–17977 (2019). https://doi.org/10.1021/jacs.9b09181
54. J. Zhou, W. Wang, L. Jing, S.-L. Chen, S.-L. Chen, S.-L. Chen, Dual-modal imaging with non-contact photoacoustic microscopy and fluorescence microscopy. Opt. Lett. **46**, 997–1000 (2021). https://doi.org/10.1364/OL.417273